

1 Documenting the Most Disastrous Landslide of 30th July 2024 Wayanad, India

2 Ali P. Yunus^{1*}, K.S. Sajinkumar², Girish Gopinath³, Srikrishnan Siva Subramanian⁴, Sahil
3 Kaushal¹, Jiyadh Thanveer⁴, A.L. Achu³, Shah Masud Ul Islam¹, Adin Ishan¹, V.K. Krishnapriya²,
4 A. Rajaneesh², Manish Dewrari⁴, Sudhanshu Dixit⁴, Shiwam Singh⁴, Piyush Srivastava⁴, Thomas
5 Oommen⁵, Nikhil Nedumpallile-Vasu⁶, Sumit Sen⁴, A.C. Narayana⁷, V. Ambili⁸, G.S. Pradeep⁹,
6 Sekhar Lukose Kuriakose⁹

7

8 ¹Department of Earth and Environmental Sciences, Indian Institute of Science Education and
9 Research Mohali, Punjab 140 306, India

10 ²Department of Geology, University of Kerala, Thiruvananthapuram 695581, India

11 ³Department of Climate Variability & Aquatic Ecosystems, Kerala University of Fisheries and
12 Ocean Studies, Kochi 682 508, India

13 ⁴Centre of Excellence in Disaster Mitigation & Management, Indian Institute of Technology
14 Roorkee, Uttarakhand 247667, India

15 ⁵Department of Geology and Geological Engineering, University of Mississippi, Oxford, MS3
16 8677, USA

17 ⁶British Geological Survey, Multi-hazard Risk and Resilience, Nottingham, United Kingdom of
18 Great Britain

19 ⁷Centre for Earth, Ocean and Atmospheric Sciences, University of Hyderabad, Hyderabad
20 502046, India

21 ⁸Geological Survey of India, Thiruvananthapuram 695013, India

22 ⁹Kerala State Disaster Management Authority, Thiruvananthapuram 695004, India

23 *Correspondence to: yunusp@iisermohali.ac.in

24

25 Abstract

26 On the morning of July 30, 2024, a catastrophic landslide struck Wayanad, India, in the
27 ecologically sensitive Western Ghats, claiming over 200 lives, with many still missing beneath the
28 debris. Here, we present a comprehensive overview of the landslide event based on field, satellite
29 images analysis, numerical modeling, geotechnical testing and aerial surveys to unravel the
30 failure mechanism and its catastrophic impact downstream. We found that a preexisting crack
31 developed in the source area in 2020, underlying complex geology, with sheared rocks and
32 structural discontinuities contributes mainly to the failure causes, exacerbated by excessive
33 rainfall. Water infiltration through cracks and joint sets in the gneissic complex led to severe
34 weathering and erosion, with soil thickness exceeding 30 m, increased susceptibility to such an
35 event. Simulations show the debris flows initiated around 01:00 hrs and peaked at approximately
36 04:00 hrs on 30 July 2024, and reached a maximum velocity of 28 m/s. The volume of the eroded
37 materials from the event was estimated as $5.17 \times 10^6 - 5.72 \times 10^6$ m³, ranking it one of India's
38 largest debris flows. The debris flow runup height in the transitional (deposition dominant) zone
39 (up to 32 m) was enhanced by multiple damming effects and entrainment, and topographic
40 attributes such as cascades and river sinuosity, causing extensive infrastructure damage. Given

41 the terrain's known fragility and history of sequential events, this region requires special attention
42 and real-time monitoring systems to mitigate future risks.

43 **Keywords:** Wayanad Landslide, Western Ghats, Climate Change, Early Warning, Debris Flow.

44 **1 Introduction**

45 Landslides are recognized as a significant natural disaster globally, posing serious threats in
46 mountainous and hilly regions (Guzzetti, 2000; Froude and Petley, 2018). Large landslide events
47 can lead to devastating consequences, including loss of life, destruction of infrastructure, and
48 long-term environmental damage (e.g., Petley, 2012; Klose et al., 2014; Fan et al., 2021; Shugar
49 et al., 2021). As such, understanding and mitigating landslide risks is crucial for communities in
50 vulnerable areas around the world. Documenting landslides is therefore of paramount importance
51 because the information obtained from the available interpretable data provides a baseline for
52 mitigation measures (Cruden, 1991; Gutiérrez et al., 2010; Guzzetti et al., 2012). The
53 documentation process involves a detailed description of essential geomorphological features,
54 geotechnical characterization, material displacement and volume, and geological and
55 hydrological conditions prevailing in the region (e.g., van Westen and Getahun, 2003; Abolmasov
56 et al., 2015; Linder et al., 2016; Dai et al., 2020). The impact of the event is largely determined by
57 the runout distance, depositional environment, and vulnerable elements in its path (Dai et al.,
58 2002).

59 The landslide documentation process traditionally relies on extensive field visits by expert
60 geomorphologists, geologists, and engineering geologists. Mapping the landslide features in a
61 field environment is often challenging due to inaccessibility, near-vertical slopes in the source
62 regions, and adverse climatic conditions. To overcome this limitation, satellite remote sensing has
63 been increasingly employed over the past few decades with technologies ranging from high-
64 resolution optical images to synthetic aperture radar (SAR) techniques (Lissak et al., 2020).
65 Despite their popularity, characterization of geologic boundaries and material characteristics,
66 even with the high-resolution satellite imagery is challenging. In particular, fracturing, joints and
67 cracks if any, and the grain sizes of debris materials at a landslide site may not be distinguished
68 with such images. On the other hand, ground-based Terrestrial Laser Scanners (TLS), and
69 Unmanned Aerial Vehicle (UAV)-based photogrammetric, and Light Detection and Ranging
70 (LiDAR) surveys have become integral to geomorphic mapping, allowing for a more precise
71 quantification of landslide processes (Niethammer et al., 2012; Lindner et al., 2016; Valkaniotis
72 et al., 2018).

73
74 Among them, RGB cameras and LiDAR sensors mounted on the UAV platform offer a versatile
75 remote sensing platform for landslide studies, as they provide operational flexibility and cost-
76 effectiveness, and can capture super-resolution images with geotagging at real-time kinematic
77 precision over steep inaccessible terrain, making them an invaluable tool for accurate and efficient
78 landslide documentation (Rothmund et al., 2017; Cheng et al., 2021; Lin et al., 2021). The
79 resulting orthophotos, LiDAR point clouds and processed digital surface and terrain models offer
80 a detailed assessment of the landslide events.

81
82 Here, we document the catastrophic landslide that occurred on July 30, 2024, between 1 am and
83 1.15 am in Meppadi Grama Panchayath, Vythiri Taluk, Wayanad district of Kerala, India, utilizing
84 field observations, image interpretations, laboratory geotechnical tests, numerical modeling and
85 UAV-based LiDAR and photogrammetric mapping techniques. The landslide originated in a
86 densely forested topographic hollow of a first-order stream and flowed through Punapuzha stream
87 that originates in Aranamala Hills (Basak and Prasad, 1989). This stream is a known debris flow

88 torrent and a tributary of the Chaliyar River, a steep-gradient fluvial system originating from the
89 Western Ghats, India.
90

91 **2 Wayanad Landslide of July 30, 2024**

92 The crown of the landslide was located at 76.134982°E longitude and 11.465104°N latitude (Fig.
93 1). The debris flow impacted Punchirimattam, Mundakkai and Chooralmala settlements along the
94 river bank. The landslide generated a huge quantity of sediments and the runout distance
95 measured from the satellite data is about 8 km, with devastating effect in these three villages. The
96 immediate trigger for the debris flow was an extreme rainfall event. The nearest weather station
97 reported 586 mm of rainfall on July 29-30, 2024, which represents about 6% of the region's annual
98 precipitation in just two days (Fig. 2). This intensity of rainfall was unprecedented for the area,
99 revealing gaps in the existing rainfall forecasting systems, which failed to predict such an extreme
100 rainfall event.

101
102 According to the estimates, 239 people were killed, 59 are missing and 1555 houses were
103 destroyed (Fig. 1). The source region of this event is known to generate deep seated landslides
104 with long runouts. The crown of this landslide covers an area officially notified as a landslide high
105 hazard zone (KSDMA, 2014; MGP, 2019), and was reiterated through previous studies (e.g.,
106 Yunus et al., 2021; Sajinkumar and Oommen, 2021; Achu et al., 2024), but the runout distance
107 was unprecedented, leading to the massive destruction downstream (Fig. 1). This necessitates a
108 reassessment of hazard mapping with inclusion of debris flow runout zones for landuse planning
109 in landslide susceptible areas.



110
 111
 112 Figure 1. Map showing the location of Wayanad Landslide. (a) Landslide scarp area reveals
 113 evidence of a planar rock slide. Large boulders remain below the crown, posing a potential risk
 114 for future, especially during periods of heavy rainfall.
 115 During the extreme rainfall event of 2020, a comparatively smaller landslide originated from the
 116 same source region, and its runout length reached ~5 km downstream, but was mostly confined
 117 within the riverbanks. The primary destruction from this 2024 July event is believed to have been

118 caused by a cascading chain of geological processes, including the damming effect. The rainfall
119 was highly localized, likely due to the orographic effects. Most of the significant rainfall occurred
120 during the evening of July 29 and the morning of July 30, 2024 (Fig. 2).

121

122 **3 Data and Methods**

123 Field and UAV survey of the landslide site was conducted during August 24 to 26, 2024, utilizing
124 a DJI Matrice 300 equipped with a Zenmuse L1 sensor for LiDAR and photogrammetric data
125 collection. Simultaneously, ground-based surveys were performed using an iPhone 15 Pro Max
126 with LiDAR capability and PiX4D Catch software to enable detailed 3D geological mapping. The
127 survey involved a total of six UAV flights, capturing over 980 high-resolution images and six sets
128 of LiDAR point clouds, providing comprehensive vertical coverage of the landslide area.

129

130 The flights were conducted at an altitude of 120 m above ground, with terrain-following mode
131 enabled to ensure consistent data acquisition over the uneven landscape. The LiDAR point clouds
132 and images were processed using DJI Terra and RGB photogrammetry, and Agisoft Photoscan
133 software, resulting in a high-density point cloud dataset containing 24 million points. This data
134 enabled the generation of a detailed orthomosaic with a resolution of 0.03 m and a digital surface
135 model (DSM) with pixel dimensions of 0.12 m.

136

137 Resultant high-resolution orthomosaic allowed for an in-depth visual analysis of the landslide's
138 characteristics, including material properties such as grain size distribution, offering an accurate
139 and comprehensive representation of both the landslide and its hinterland. By overlaying the
140 orthomosaics on a shaded relief map, subtle surface geological features were revealed,
141 highlighting zones of weakness and potential instability.

142 The digital elevation model (DEM) generated from the survey data was crucial in detecting and
143 quantifying morphological changes within the landslide zone. By comparing the post-event DEM
144 with pre-event DEMs, sourced from ALOS PALSAR a 12.5 m spatial resolution elevation data,
145 we were able to quantify the total volume of material eroded during the landslide event. This
146 information is critical for understanding the dynamics of the landslide and assessing future risks
147 related to erosion and slope stability.

148

149 Soil depths were measured using a Nikon laser rangefinder measurement using 2-point analysis.
150 For the grain size analysis, we employed BASEGRAIN software developed by Martin Detert at
151 the River Engineering division of the Laboratory of Hydraulics, Hydrology and Glaciology of the
152 Swiss Federal Institute of Technology (ETH) at Zurich, Switzerland. This software follows Fehr's
153 line-sampling method (Fehr, 1987). Methodological aspects of BASEGRAIN are described in
154 detail in Detert and Weitbrecht (2013), and are available to download from the ETHZ repository:
155 <https://basement.ethz.ch/download/tools/basegrain.html>. Additionally, we collected undisturbed
156 (from the valley sides) and disturbed soil/debris samples from different locations across the debris
157 flow deposits close to the fan. The samples were transported to the laboratories for geotechnical
158 testing. Types of minerals in the undisturbed soil samples were determined through X-ray
159 diffraction (XRD) analysis. The mineral composition was identified by comparing the peak
160 intensity positions (2θ) in the sample's X-ray diffraction pattern with the reference peak positions
161 from the Joint Committee for Powder Diffraction Standards (JCPDS).

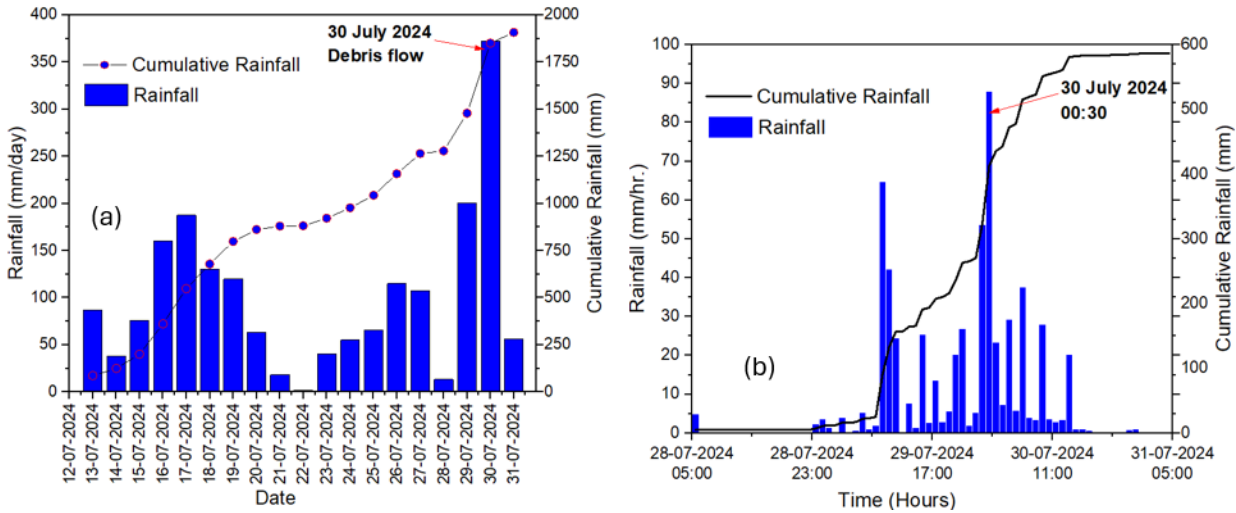
162

163 Using samples collected from the debris flow deposits in Wayanad, we perform index,
164 hydrological and geotechnical property tests, i.e., laboratory-sieved grain sizes, hydraulic
165 conductivity at saturated state, and shear strength at unsaturated states. The minimum depth of
166 the debris beds is 6 m, and the maximum value of matric suction the test can consider is 80 kPa

167 (~8 m). We chose 30 kPa and 40 kPa to consider the unsaturated behaviors of the bed materials
168 at 3 m and 4 m depths.

169
170 To model the initiation and timing of the debris flow, we gathered daily rainfall data from the
171 nearest meteorological station, Kalladi (~8 km from the source), via the Kerala WRIS web page
172 (<https://wris.kerala.gov.in/mis/wd/home/rainfall-actual>). However, determining the precise start
173 time of the landslides requires hourly rainfall data, which is essential for accurately interpreting
174 the disaster. To address this, we used cumulative daily rainfall observations and trends from the
175 GPMV8 satellite for July 28–31, 2024, to estimate hourly rainfall. We then adjusted the hourly
176 data to match the observed cumulative total of approximately 586 mm (Fig. 2). This data was then
177 used in a spatially distributed model that simulates rainfall-induced landslides and debris flows
178 (Dixit et al. 2024), with the parameters described in Table S1, which simulated a 72-hour period
179 from 28 July 2024, 05:30 AM to 30 July 2024, 05:30 AM. The model assumes the Mohr-Coulomb
180 failure criterion to model the stability of rock-debris masses near the crown portion of the landslide.
181 The safety factor is assessed using the Mohr-Coulomb linearly elastic perfectly plastic material
182 constitutive model applicable to geomaterials soils and rock.

183 For modeling debris flow velocity, we employed a RAMMS model that simulates debris flow using
184 depth-averaged shallow water equations, specifically in its single-phase configuration (RAMMS,
185 2017; Mikoš and Bezak, 2021). The model incorporates the Voellmy-fluid friction model and
186 requires dry Coulomb-type friction (μ) and viscous-turbulent friction (ξ). We assigned a value of
187 0.01 for μ and 100 m/s is assigned for ξ , following literature (Mikoš and Bezak, 2021), and trial
188 and error calculations. A comprehensive explanation of the model's theoretical framework and
189 governing equations is available in the user manual.



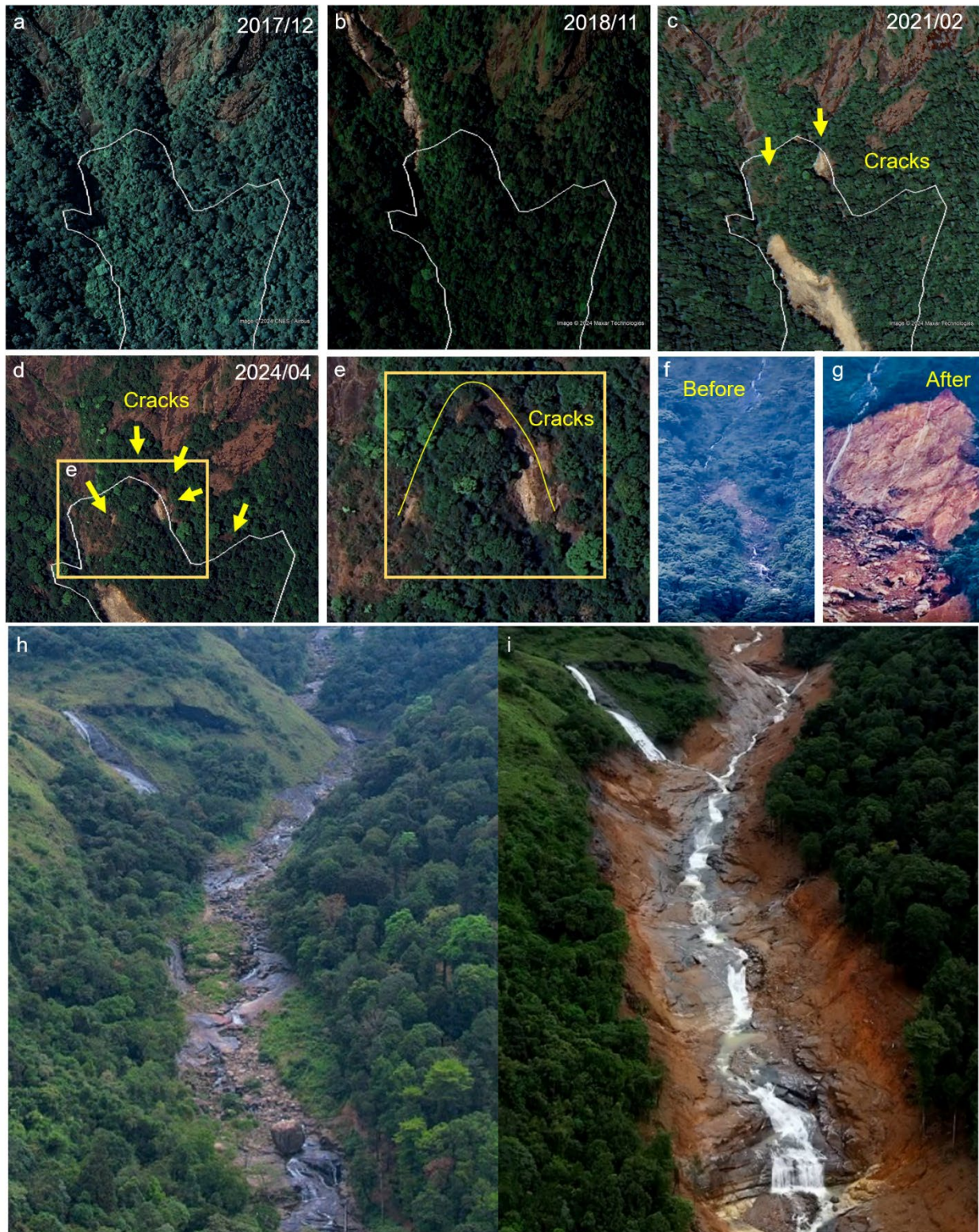
190
191 Figure 2. (a) Daily rainfall at Kalladi station (data from Kerala-WRIS), and (b) corrected hourly
192 rainfall data.

193 **4 Results**

194 **4.1 Landslide origin and morphology**

195 The catastrophic landslide that occurred on July 30, 2024, involved a planar sliding of rock masses
196 from a steep section of the Western Ghats slopes (Fig. 1). We attribute the cause of this rock
197 failure to the 2020 landslide and its subsequent downslope movement (Fig. 3b-d). This movement
198 caused a fracture to open in the upper slope, extending into the underlying bedrock and widening
199 over time (Fig. 3c-e). In the fractured zone, the slope is particularly steep, with gradients reaching

200 as high as 60% over a horizontal distance of 150 m from the crown, corresponding to an elevation
201 gain of about 90 m. During the intense rainfall on July 29 and 30, 2024, water infiltrated these
202 fractures, saturating the slope and increasing its instability. The increased water pressure finally
203 led to a sudden failure of the rock mass along these cracks (see Fig 3e), on 30th July 2024, and
204 rapidly descended toward the valley bottom (Fig. 1a).



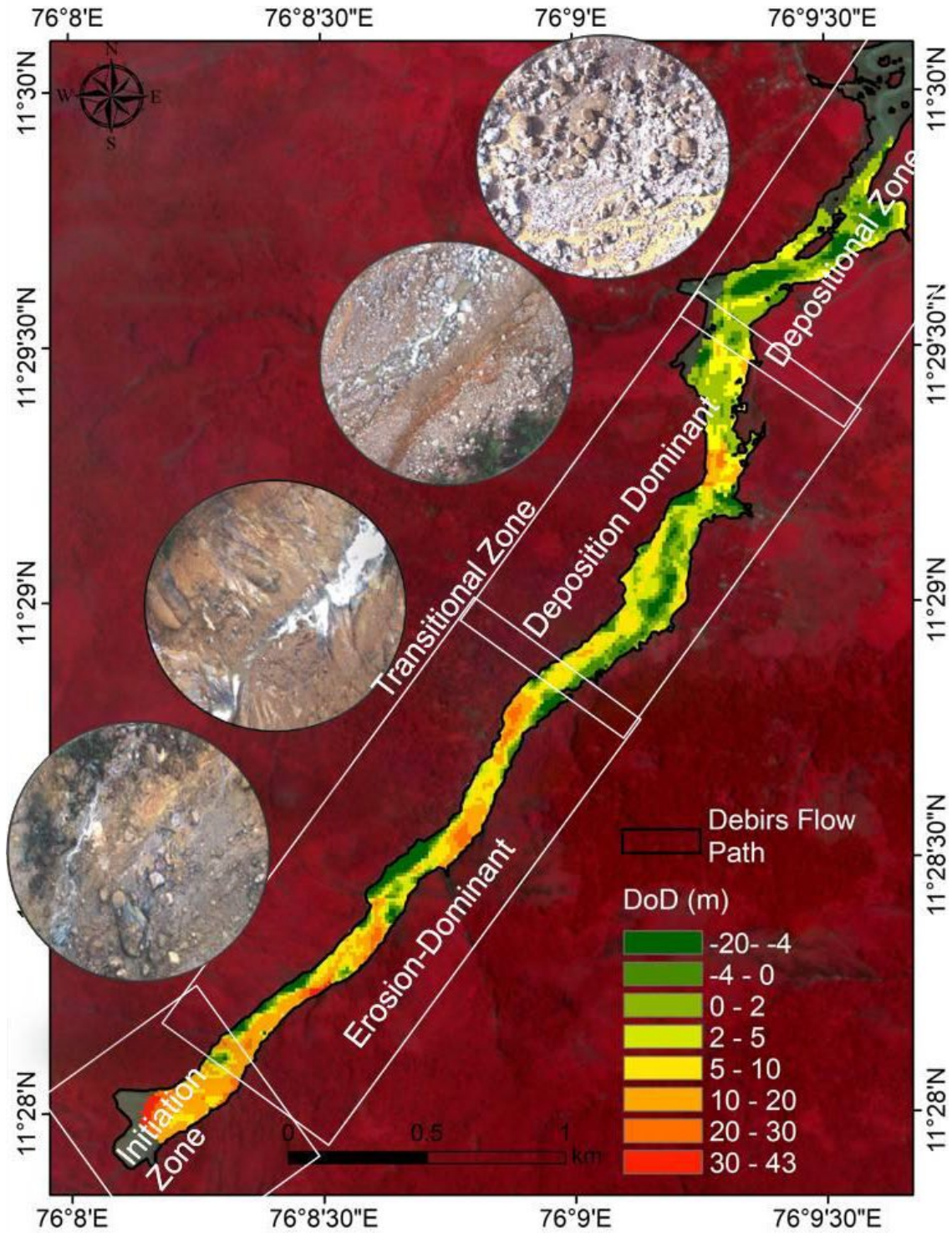
205
 206 Figure 3. (a) Satellite image of December 2017 showing the landslide source area (marked in
 207 white polyline) without any disturbance, (b) a minor debris flow in the top of source area after the
 208 2018 monsoon, image captured in November 2018; (c) showing the satellite image of February
 209 2021, showing a major debris flow (happened in 2020 monsoon) in the source area, along with

210 the cracks developed due to slope destabilization; (d) and (e) showing satellite image few months
211 before the 2024 debris flow with widened cracks. Aerial view of the landslide source and transition
212 zone before (f, h) and after (g, i) the July 30, 2024 event (images reused with permission from
213 Shagin Sunny and Vishnu KM)

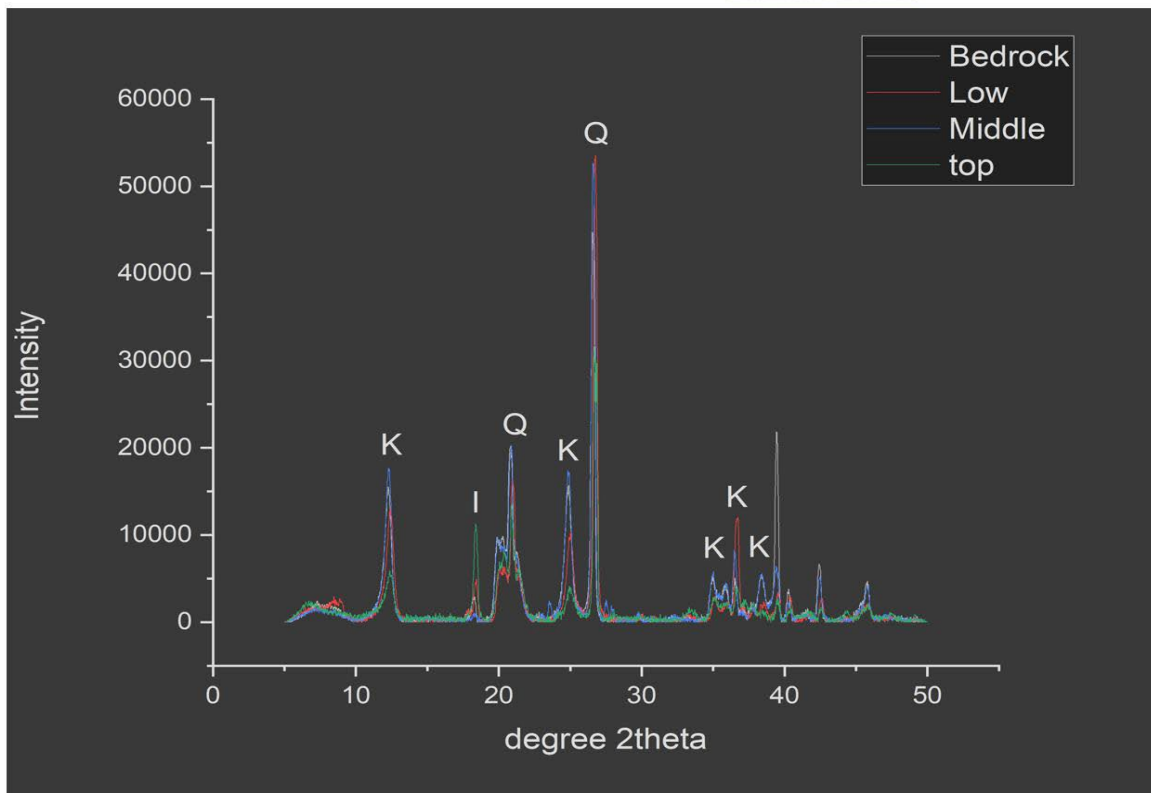
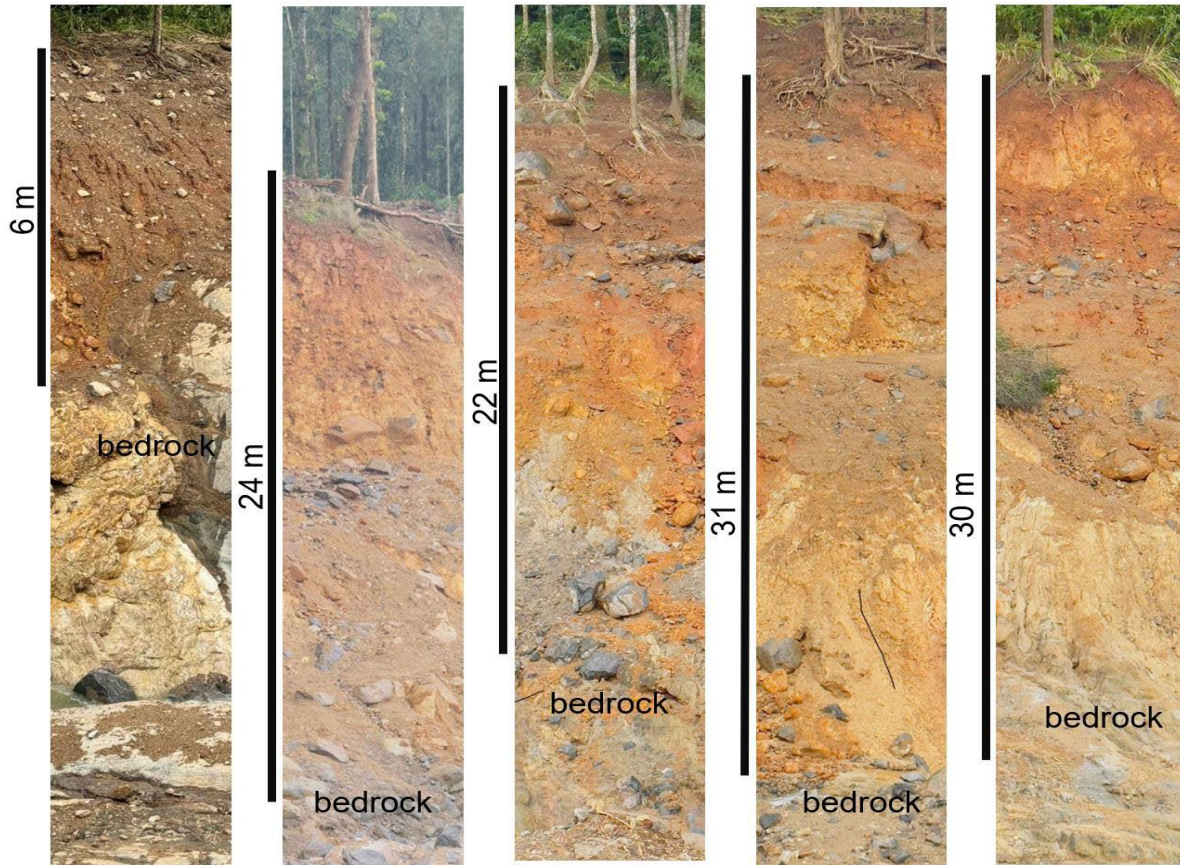
214
215 This event produced a mix of large boulders, soil, and uprooted vegetation (Fig. S1), which were
216 transported further downslope, driven primarily by gushing rainwater and transformed into a highly
217 mobile debris flow. Local reports suggest that the landslide occurred in two phases. The first event
218 was reported around 1:00 – 1.15 AM on the morning of July 30, followed by a second event
219 around 4:00 AM. This sequence of events has led to the hypothesis that the initial slide may have
220 caused the debris to form temporary blockage and damming effect in the river. The location of
221 probable damming sites is shown in Figure S2a-c, corresponding to: (i) a narrow section of the
222 river channel, (ii) the Punchirimmattam bridge and (iii) behind Seethammakund waterfalls, verified
223 by field observation. These temporary dams' eventual failures, releasing a larger volume of
224 material downstream causing enhanced runoff and catastrophic devastation downstream.

225
226 Based on field observations and detailed analysis of the ortho-mosaic, the landslide area has
227 been divided into four distinct zones: (i) the initiation zone, (ii) the erosion-dominant transitional
228 zone, (iii) the deposition-dominant transitional zone, and (iv) the deposition zone (Fig. 4). Field
229 data suggest that the initiation zone is characterized by an average soil thickness of about 6 m,
230 below which the weathered rock layers are structurally weak and jointed. In the transitional zones,
231 the soil thickness ranges from 10 to 33 m, as observed from a laser range finder measurement
232 (Fig. 5).

233
234



235
 236 Figure 4. DEM of Difference (DoD) estimated from ALOS Palsar 12.5 m DEM and UAV DEM for
 237 the study area. Negative values (green color) represent deposition and positive values represent
 238 (yellow to red) erosion. Background FCC is sourced from PlanetLabs.



240 Figure 5. Top panel: Soil thickness observed for the study area (measured using a laser range
241 finder). Bottom: X-ray diffraction patterns of the soil (top soil, middle, bottom and from bedrock
242 contact) analysed for the study area

243

244 **4.2 Geological and structural fragility leading to the disaster**

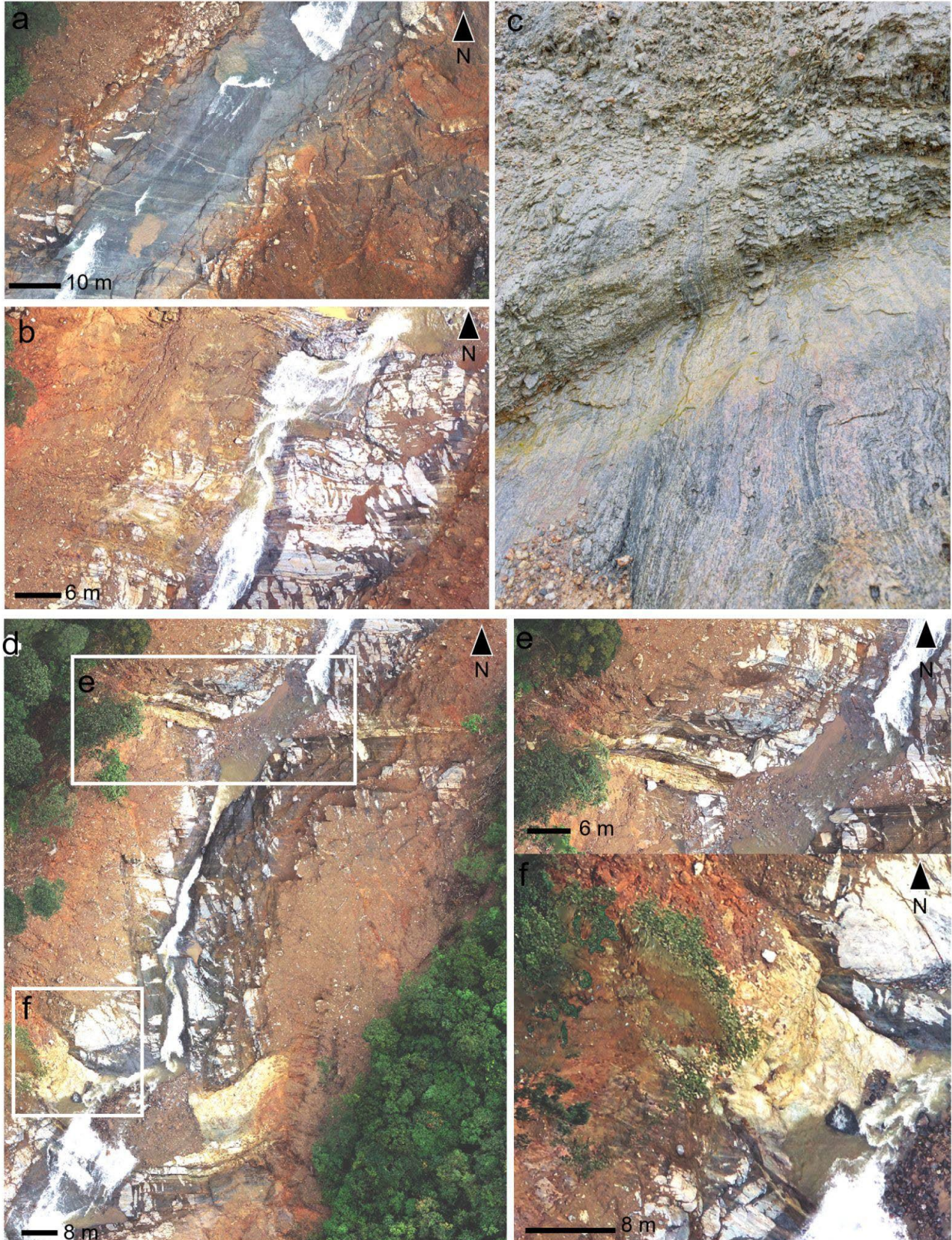
245 The region has been extensively mapped by the Geological Survey of India (GSI), identifying it
246 as a part of the Southern Granulite Terrain (SGT). This terrain is characterized by gneissic
247 complex and charnockite, with the primary lithological units being garnet-biotite gneiss and
248 garnet-biotite-hypersthene gneiss. Following the landslide event, the outcrop has been
249 significantly exposed, allowing UAVs to capture fine-scale details of the lithological and structural
250 features (Figure 6a-c).

251

252 The rocks in this area experience intense weathering and shearing in various locations (Figures
253 6d-f). Due to the high feldspar content in these litho-units, they weather more rapidly, transforming
254 into kaolin—a clay-rich soil (Fig. 5). As a result, the region has developed a substantial soil
255 thickness (Fig. 5, Fig. S3), which further contributes to the area's susceptibility to landslides and
256 erosion.

257

258



259
 260
 261

Figure 6. (a) Unweathered (76.145971°E, 11.475760°N), and (b) weathered and sheared (76.147987°E, 11.479210°N) gneiss exposed in the river valley observed from UAV. (c) field

262 photograph showing the weathered and unweathered part of gneiss (note the pink coloration in
263 gneiss by large feldspar content), (d-f) presence of shearing in multiple places that resulted in
264 extensive weathering of the host rocks, and formation of localized knickpoints.

265
266 Another significant geological feature of the field site is the well-defined system of joints visible in
267 the exposed outcrops (Fig. 7). Three distinct sets of joints are present, with the most prominent
268 set oriented along N250°/35S. The vertical joints along the gneissosity created large blocks by
269 the parallel set of joints. These joint systems play a crucial role in shaping the geomorphology of
270 the area, as the river actively erodes along these joints, resulting in noticeable shifts in its course
271 (Fig. S4). Ambili and Narayana (2022) reported that landslides in the region are concentrated
272 along crustal-scale lineaments trending NW-SE and NE-SW. These lineaments form a conjugate
273 set of smaller fractures, which serve as conduits for groundwater seepage, contributing to slope
274 instability. Along with the brief period of water damming in the higher reaches, the substantial
275 overburden could have produced extra pore pressure in the area's steeply foliated rocks, creating
276 a tremendous amount of potential and kinetic energy.

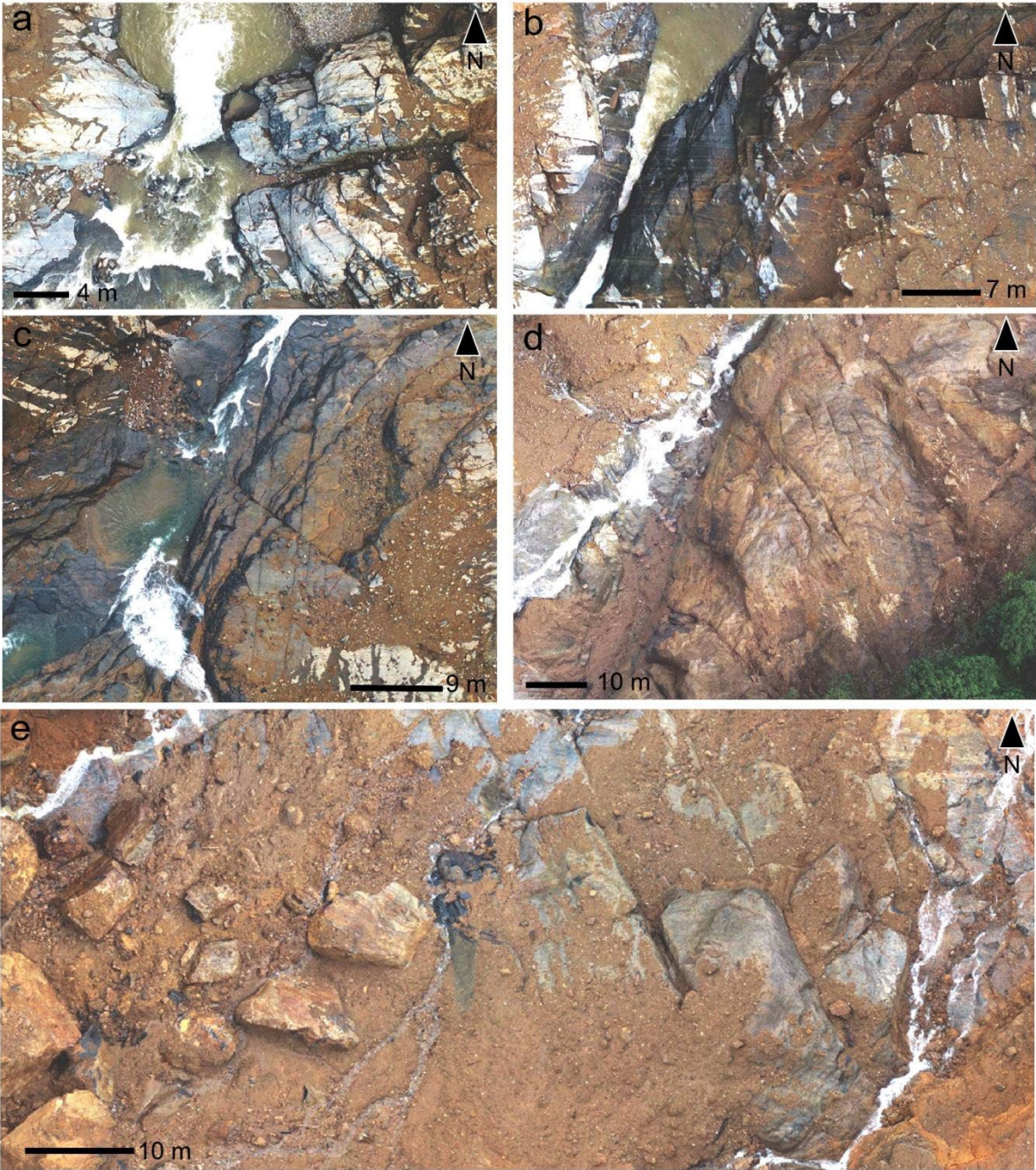
277
278 Field analysis has also uncovered several instances of historical debris flow deposits in the area.
279 Boulders of various sizes and shapes, which are characteristic of past debris flows, have been
280 observed in the lower reaches of the river valley (Fig. S5 – S6). These deposits indicate a long
281 history of debris flow activity in the region, suggesting that such events have been occurring over
282 an extended period. The presence of such markers highlights the region's susceptibility to debris
283 flows and provides valuable insight into the recurring nature of these geological processes.

284
285 **4.3 Landslide volume and channel morphological changes**
286 The differencing of digital elevation models (DoD) provided crucial insights into landscape
287 changes following the July 2024 Wayanad debris flow, revealing both the extent of erosion and
288 deposition in the affected valley (Fig. 4). DoD analysis indicates that the total volume of eroded
289 material from the source and transitional areas is between $5.1 \times 10^6 \text{ m}^3$ and $5.7 \times 10^6 \text{ m}^3$. The
290 uppermost section of the valley experienced significant erosion, with depths ranging from 30 to
291 40 meters, affecting both soil and bedrock layers (Fig. 8a-b).

292
293 To assess the morphological changes in detail, multiple cross-sections were generated and
294 compared with DoD data derived from ALOS PALSAR and UAV DEM. The debris flow, initiated
295 in the source area, transitioned into the valley, profoundly altering the valley floor and sides.
296 Extensive erosion of weathered rocks led to the widening and deepening of the valley (Fig. 8c-d).
297 In the erosion-dominant transitional zone, erosion depths varied between 10 and 30 m (Fig. 4).

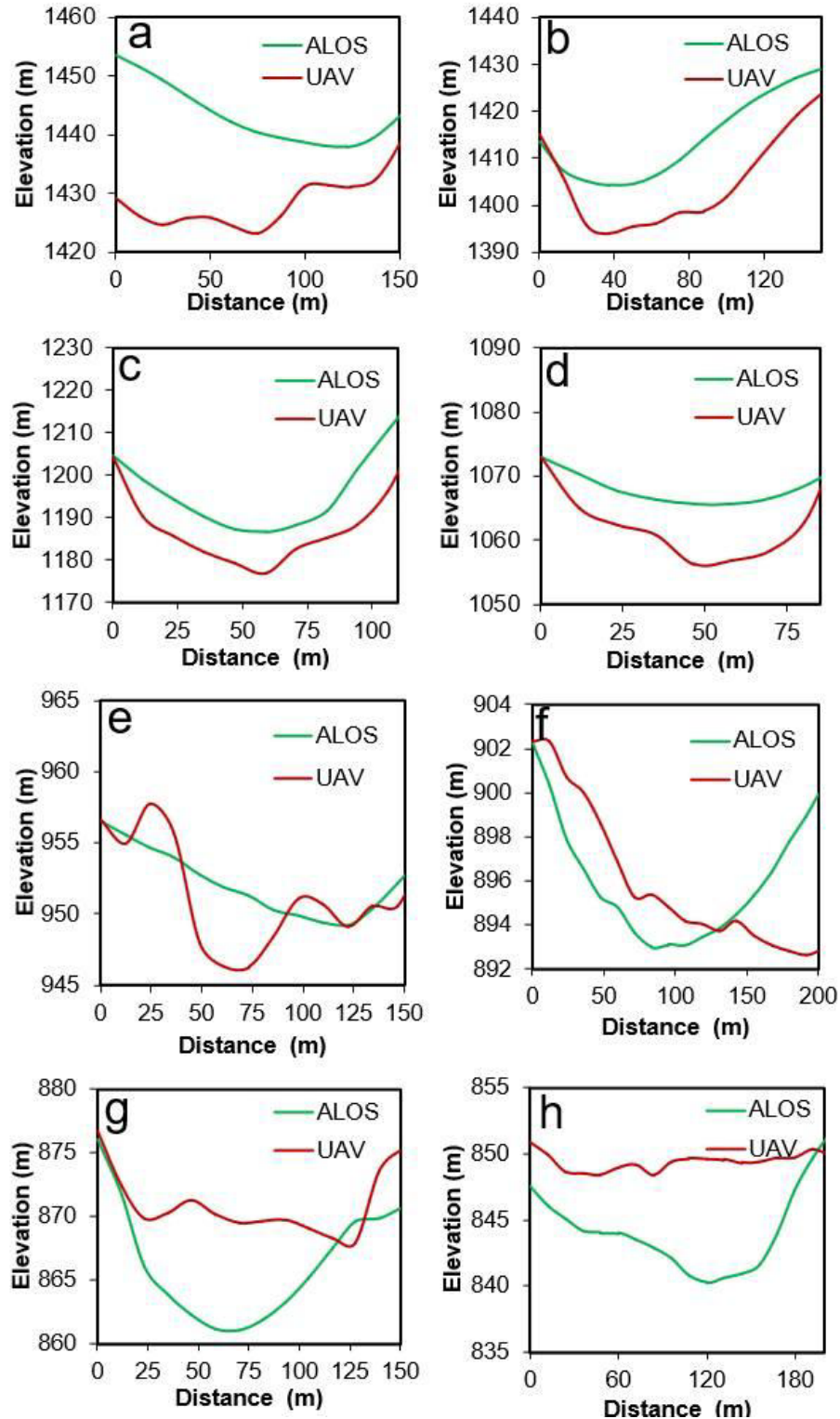
298
299 In the deposition-dominant transitional zone, where the flow lost energy, the depositional
300 thickness was measured at 2-10 m, while erosion was limited to less than 10 m (Fig. 8e-f). As the
301 mass moved downstream, it exhibited significant runup, with debris materials reaching up to 28-
302 32 m above the valley floor in certain sections (Fig. 9), which caused widespread destruction to
303 the infrastructures. Clear trim lines like features, visible at various heights along the flow path,
304 mark the limits of the debris movement, showing the destructive power of the event (Fig 9). The
305 maximum recorded deposition thickness in the lower valley reached up to 16 m, indicating
306 substantial material accumulation in this area (Fig. 8g-h).

307
308



309
 310
 311
 312
 313

Figure 7. Prominent joint sets displayed in the study area (a) lower reaches (76.154466°E, 11.486922°N), (b, c) middle reaches (76.147870°E, 11.478731°N; 76.145576°E, 11.475143°N) and (d and e) upper reaches (76.142184°E, 11.471134°N; 76.137601°E, 11.467423°N).



314
 315 Figure 8. Channel cross sections are drawn at initiation zone (a and b), transitional zone – erosion
 316 dominant (c and d), transitional zone – deposition dominant (e and f), and depositional zone (g
 317 and h).

318
 319 Long profile analysis shows several cascades (knickpoints) in the study area, likely formed as a
 320 result of the shearing and weathering processes that created alternating hard and soft rock layers

321 (Fig. S7). These cascades originated due to differential erosion, as seen in figure 6d in the
322 sheared location, where the softer (sheared) layers eroded more rapidly than the harder ones,
323 creating stepped profiles along the slopes. During the catastrophic debris flow on July 30, 2024,
324 these cascades also have played a critical role in exacerbating the flow's destructiveness. As the
325 debris, including large rock boulders, soil, and uprooted vegetation, moved downslope, the
326 cascades acted as points of increased energy dissipation. This turbulent flow over the cascades
327 would have caused the debris to accelerate, intensifying the velocity and erosive power of the
328 flow. Additionally, the cascading terrain likely fragmented the debris further, breaking large
329 boulders into smaller pieces and allowing finer materials to mix with the water, increasing the
330 mobility and spread of the debris flow.

331 332 **4.4 Run-up height**

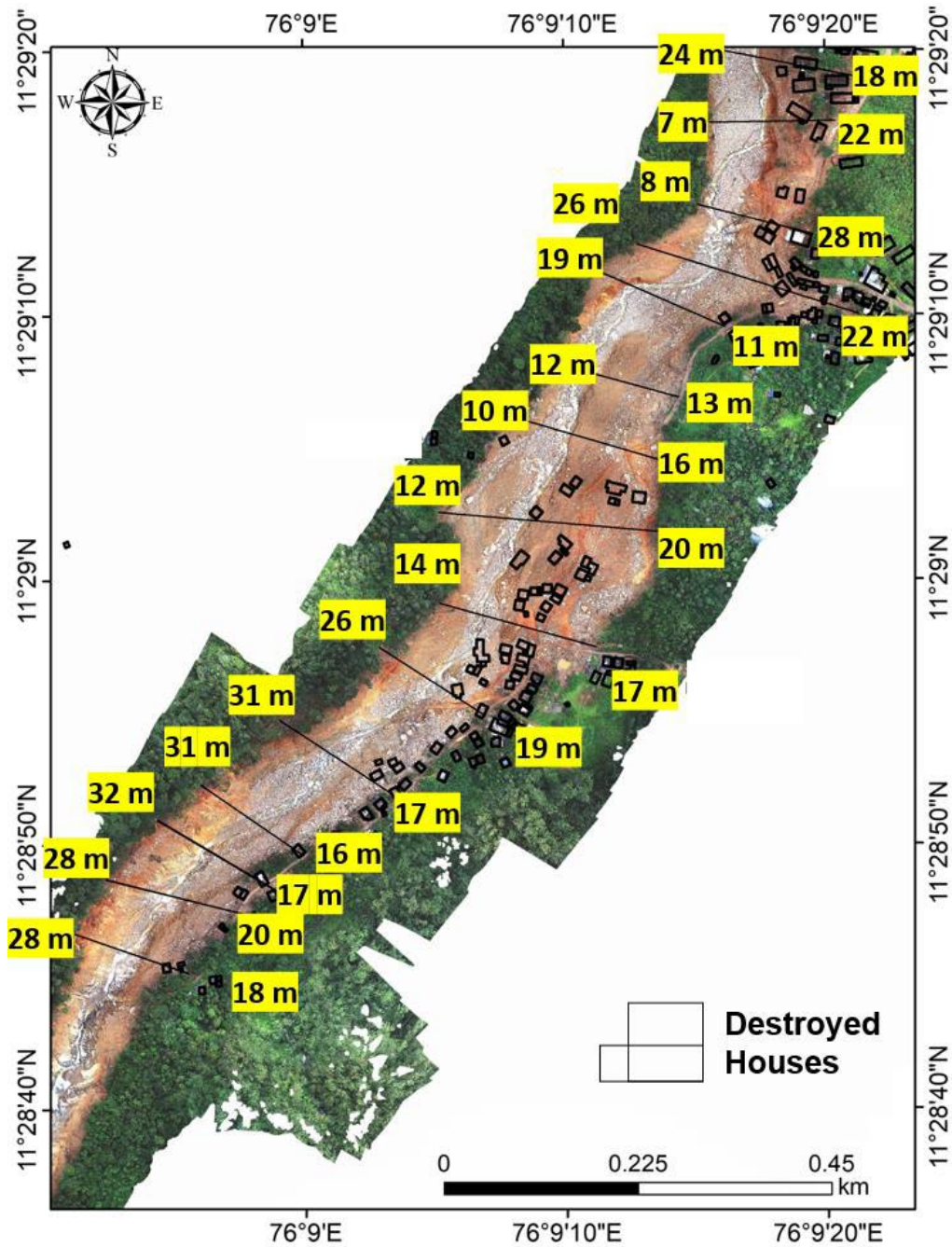
333 The devastation in the region is primarily due to the significant run-up height of the debris flow
334 and the force of the gushing water. Reports indicate that 1555 houses were destroyed as a result
335 of this catastrophic event (KSDMA). Our analysis of the run-up height, which is the vertical
336 distance the debris flow traveled up the valley walls, was estimated based on the distribution and
337 deposition of material in the transitional zone between the highest point and river channel bottom
338 (Fig. 9).

339
340 The unprecedented run-up heights of up to 32 m may be because of the damming effect. The
341 damming reduces the viscosity of the material by accumulation of rain water and therefore the
342 debris held behind it. But when the dam breaks, these materials can travel longer distances,
343 particularly when the dam is in a steep slope. Accumulation of water and collection of debris from
344 uphill may also have rapidly increased run-up heights. The velocity of the material released from
345 such landslide dams can be seen as a function of the slope and the viscosity of the material that
346 is held behind the dam. It is in effect like a dam break, but the released material has higher
347 viscosity than just rain water. Therefore, as the dam is formed, it will cause a lot of accretion on
348 the banks of the material tail. But when the dam suddenly broke it may have rapidly ventilated the
349 vadose zone and the viscous material may have scoured the sides of the runout zone leading to
350 increased material load as it went downhill. Radial cracks are seen up to 30 m on either side of
351 the landslide body in the runout zones which may be owing to such rapid ventilation of pore
352 spaces leading to consolidation of the materials and sudden removal of support that was offered
353 by the soil and trees that were in the river sides (Fig. S8). These are also potential areas of future
354 slope failures. Such observations need to be further tested in flumes. Much of these processes
355 cannot be easily simulated in laboratory and the fact that many of such landslide dams last less
356 than a day implies lack of observational evidences (Li et al., 2024).

357
358 The highest run-up heights were also observed in areas where the river bends, as these locations
359 tend to experience greater flow velocity and debris accumulation due to the centrifugal forces
360 acting on the moving mass. The maximum recorded run-up height was 32 m on the left bank and
361 28 m on the right bank where the sinuosity is highest. These extreme heights suggest that the
362 debris flow had immense energy as it surged through the narrow, curving sections of the valley,
363 exacerbating the destruction on both sides of the river.

364
365 In contrast, in broader, less confined valleys, the run-up height was comparatively lower, ranging
366 between 10 and 20 m (Fig. 9). The reduced run-up height in these areas can be attributed to the
367 wider valley geometry, which allowed the debris flow to spread out more evenly, dissipating
368 energy over a larger area and reducing the vertical reach of the material. These variations in run-
369 up height across different sections of the river indicate that the topography played a critical role
370 in influencing the intensity and distribution of the debris flow's impact. Areas with sharp river bends
371 and narrow channels were subjected to the greatest forces, leading to higher run-up heights and

372 more severe damage, while wider valley sections experienced less vertical displacement of
 373 debris, resulting in comparatively lower levels of destruction.
 374



375
 376 Figure 9. Run-up height estimated based on material deposition and valley floor height in the
 377 transitional zone – deposition dominant. Note that run-up height is maximum in river bends and
 378 lowest in flat and wide valley floors.
 379

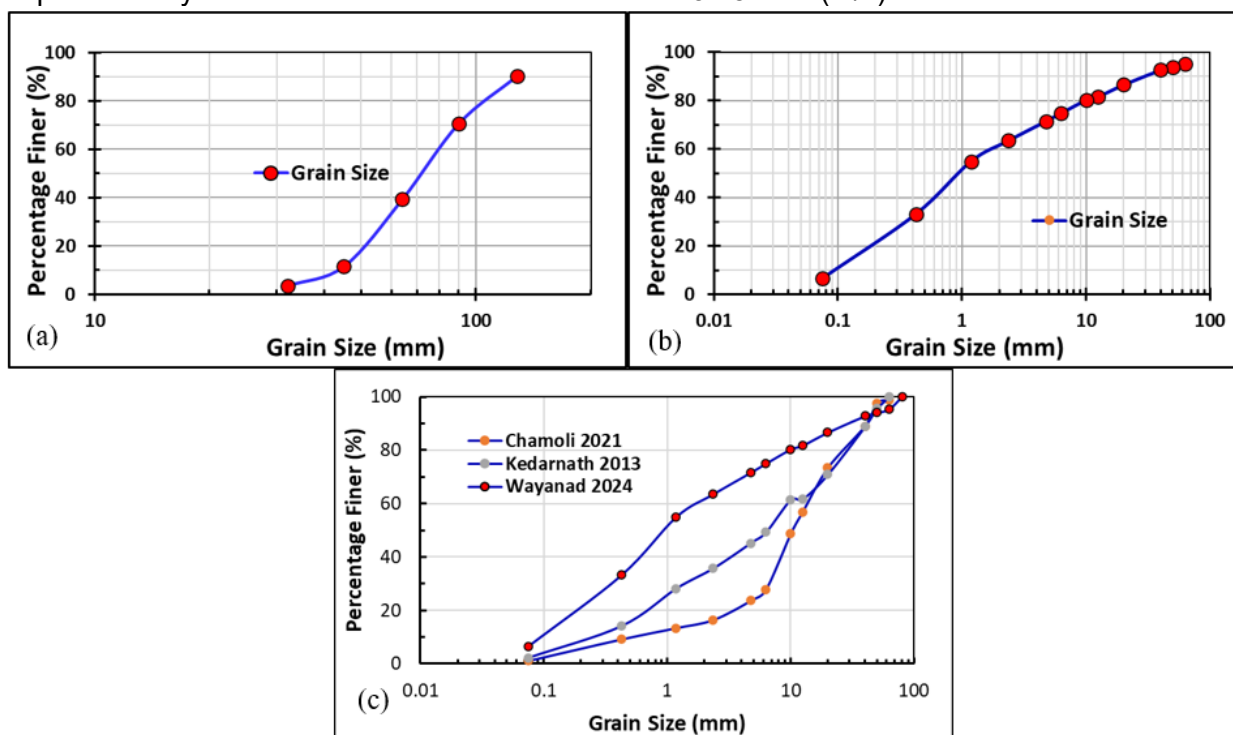
380
 381 **4.5 Grain size distribution and geotechnical characteristics**

382 In the transitional zones, where deposition dominates, substantial accumulations of large
 383 boulders, cobbles, and gravel have been observed (Fig. S9). This deposition results from the

384 deceleration of the debris flow, which occurs as the river gradient decreases. The reduced slope
 385 slows the flow velocity, causing heavier materials to settle out first. Additionally, the valley widens
 386 considerably in these zones, further contributing to the reduction in flow energy and promoting
 387 the deposition of coarser materials.
 388

389 At the point where deposition begins, the median grain size (D50) of the deposited material is
 390 approximately 135 mm, indicating the presence of large cobbles and small boulders. As the flow
 391 continues downstream, about 500 m from the transitional zone, the D50 decreases to 47 mm,
 392 reflecting a shift toward finer material as the flow loses energy (Fig. S9). And at ~1.5 km
 393 downstream from the transitional zone, the river widens significantly, developing braided
 394 characteristics and forming island bars. This area is also marked by the formation of a debris flow
 395 fan, where the rapid widening of the valley allows the flow to spread out, further reducing its
 396 velocity. The debris flow fan is characterized by the deposition of both fine and coarse materials,
 397 with large boulders and finer sediments distributed across the fan's surface as the energy of the
 398 flow dissipates. In these lower sections of the valley, the thick deposits of gravel on the valley
 399 floor exhibit median grain sizes of 32 mm and 22 mm, respectively (Fig. S9). The fan displays
 400 classic depositional features, such as lobate forms and radiating channels, which are indicative
 401 of multiple surges within the debris flow event.
 402

403 Geotechnical assessment of the soil/debris samples revealed material properties and
 404 characteristics (Fig. 10). The laboratory tested median grain size of the debris is D_{50} around 1
 405 mm. We find that the Wayand debris flow deposits are characterized by larger amounts of fine
 406 particles compared to other debris flows in the Himalayas (Fig. 10c). A falling head permeability
 407 test is performed at two different field densities 1.88 g/cc and 1.57 g/cc. The average coefficient
 408 of permeability at the saturated state is estimated as 3.75×10^{-6} (m/s).



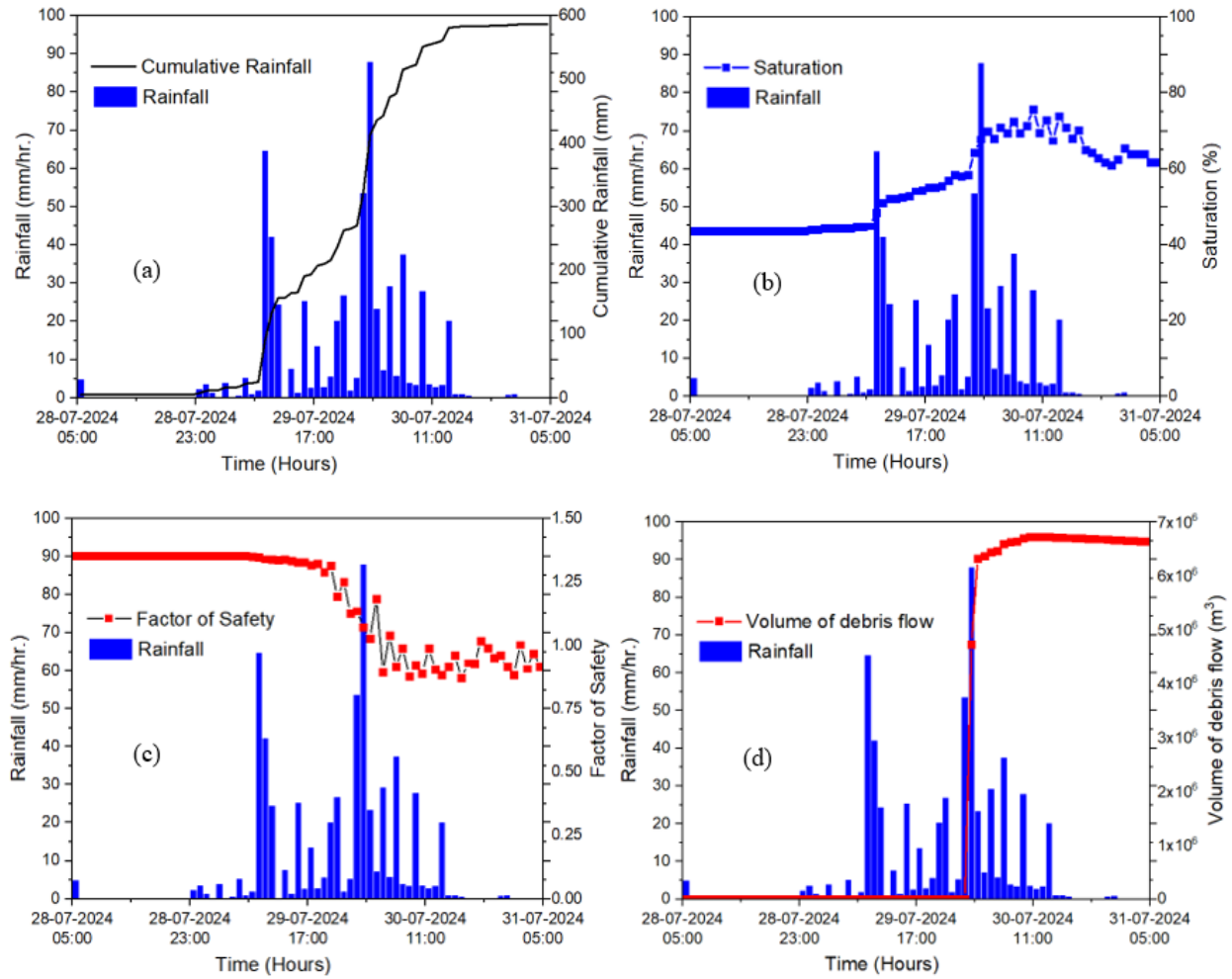
409 Figure 10. (a) Grain sizes measured using Wolman pebble count and Gravelometer scale, (b)
 410 Grain sizes obtained from sieving in the laboratory, and (c) comparison of GSDs among three
 411 debris flow deposits i.e., Kedarnath 2013, Chamoli 2021, and Wayanad 2024.
 412
 413

414 Triaxial experiments on the samples at unsaturated state at matric suction = 30 KPa, and matric
415 suction 40 KPa resulted in cohesions 24.5 KPa and 49 KPa respectively and an angle of internal
416 friction 39.7° and 36.5° respectively. Fig. S10 shows the shear strength of the samples at 30 KPa
417 matric suction (Fig. S10a) and 40 KPa matric suction (Fig. S10b) at confining stress levels 49
418 KPa, 98 KPa, and 147 KPa. A decrease in cohesion with decrease in matric suction is observed.
419

420 **4.6 Landslide dynamics from numerical simulations**

421 The numerical analysis suggests that the debris flows initiated around 01:00 and peaked at
422 approximately 04:00 on 30 July 2024 (Fig. 11). Simultaneously, the crown portion decreased
423 stability, as indicated by a drop in the Factor of Safety (FoS). The model-derived volume of the
424 debris flow at the time of the landslide was 6.32 million m^3 . A reasonable correlation was observed
425 between the model results and the DoD output.

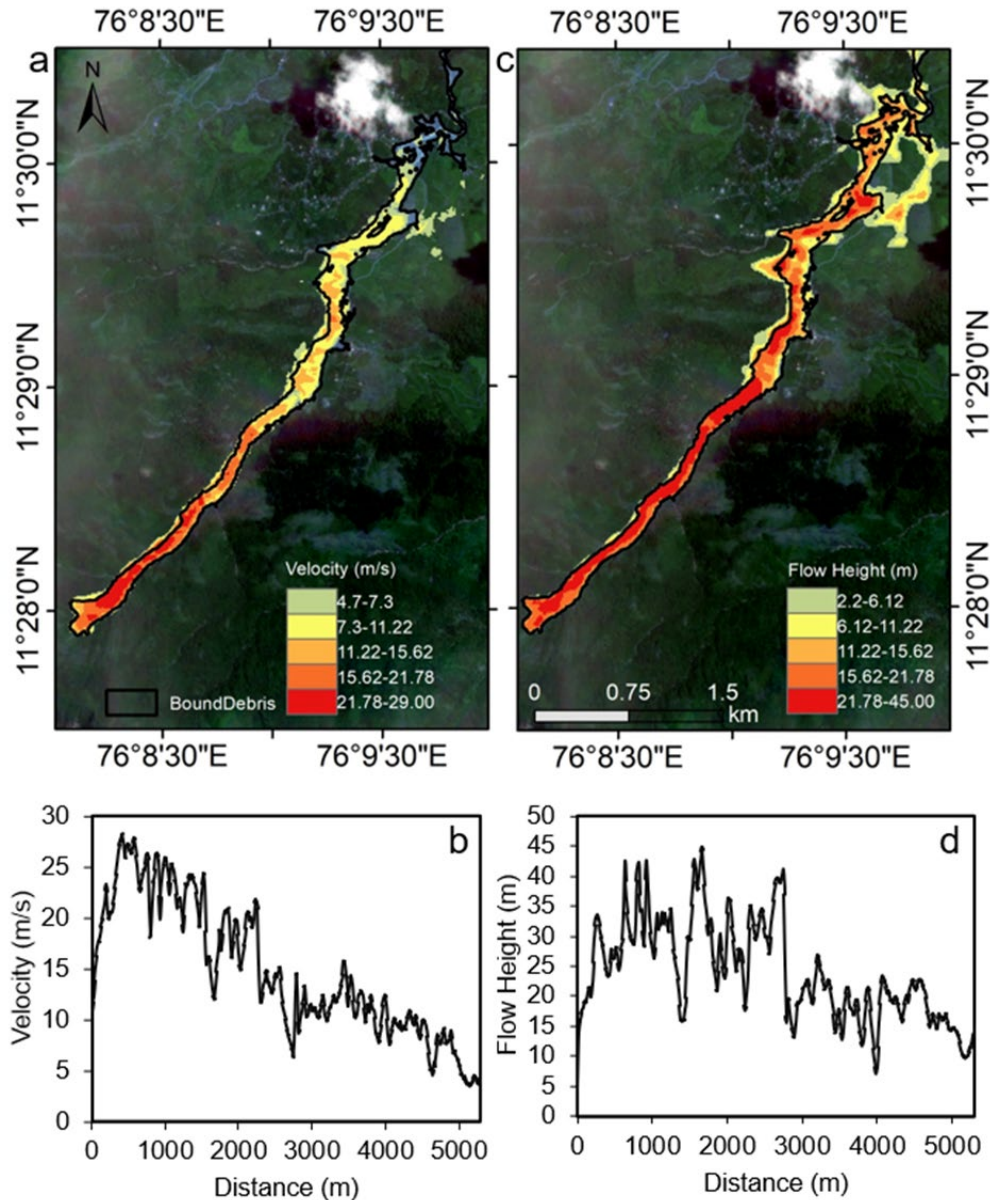
426 The RAMMS simulation predicted a maximum flow velocity of 28 m/s at about 400 m downslope
427 from the crown, marking the start of the transitional zone (see Fig. 12). As the debris flow
428 progressed, the velocity gradually decreased to 11 m/s at about 2300 m, where the valley began
429 to widen, indicating a loss of energy and deceleration. At 5000 m from the source, the velocity
430 further reduced to 5 m/s. In the absence of field data or video footage to validate these velocities,
431 we relied on flow height data from the RAMMS model to cross-check against runup heights
432 observed in DEMs. The results show a close match between simulated and observed flow heights
433 at 9 of the 15 sites (see Fig. 9 and 12), with mostly overestimation at the remaining 6 sites.



434

435 Figure 11. (a) Hourly and cumulative rainfall from 28 July to 31 July 2024, (b) Degree of saturation
 436 averaged for the catchment, (c) Factor of Safety of vs Time, and (d) Volume of debris flows (m

437



438

439 Figure 12. Debris flow velocity (a and b) and flow height (c and d) simulated for the study area
 440 employing RAMMS.

441 **5 Discussion**

442 **5.1 Wayanad 2024 event: natural vs anthropogenic debates**

443 The Western Ghats Ecology Expert Panel (WGEEP), also known as the Gadgil Commission,
 444 submitted a report in 2011 warning against anthropogenic disturbances, such as indiscriminate
 445 quarrying and construction, in the ecologically sensitive areas of the Western Ghats (Gadgil,
 446 2014). As per the report, the Western Ghats were divided into three zones—ESZ-1, ESZ-2, and
 447 ESZ-3—based on their ecological fragility, with a complete ban on quarrying, mining, and the
 448 transfer of forest land for non-forest purposes recommended for ESZ-1 areas. Following the
 449 catastrophic landslide on July 30, 2024, news debates, articles, and social media discussions

450 largely attributed the disaster to the failure of policy institutions to implement key ecological
451 recommendations from the 2011 report (Sajit, 2024; Statesman, 2024; Das, 2024; ABPLive,
452 2024).

453 However, field observations along with UAV and satellite images, show that the source area of
454 the July 30, 2024 landslide is free from any significant anthropogenic disturbances. No prominent
455 quarries or mining operations are reported within a 10-km radius of the landslide source.
456 Additionally, forest land conversion for non-forest use, such as cardamom plantations, is only
457 located about 1.5 km below the source zone. We conclusively showed that a preexisting crack
458 developed in 2020 debris flow led to a planar failure in 2024, triggered by the heavy rainfall (see
459 Fig 2 and 3).

460 Further, research by Muraleedharan (1995) and others has emphasized the connection between
461 landslides and the geological fragility of the region, particularly in structurally weak zones
462 identified during a reconnaissance survey by the Geological Survey of India following the 1984
463 Mundakkai landslide. Our study findings also point to the presence of highly fractured rock units,
464 jointed strata, and severe water induced erosion as the primary causes of landslide initiation,
465 exacerbated by the intense rainfall. Furthermore, the destructive power of the event was amplified
466 by the geomorphological features of the river valley, including cascades and the sinuous course
467 of the river (Fig. 9 and Fig. S7). Previously, Yunus et al. (2021) mapped the landslides in the
468 Chaliyar river basins following the 2018-19 monsoon rain and reported more than 50 large scale
469 debris flows, most of them originated in the uninhibited zones, and their long runout tail traveled
470 through the populated areas highlighting the terrain fragility, stream power and concavity profiles
471 as the major topographic control, rather than pointing to the anthropogenic disturbances;
472 prominent ones are Puthumala, Kavalappara and Paathar landslides, which killed several people
473 and destroyed many infrastructure downstream.

474 Furthermore, the materials in Wayanad debris flow are found prone to erosion due to the
475 abundance of finer fragments in the debris. These finer fragments might have been a result of
476 prolonged weathering and subsequent erosion by previous debris flows. The geotechnical
477 experiments performed (see section 4) using the materials sampled at the debris flow deposits
478 revealed sensitivity to variable moisture content. Loss of shear resistance is observed with
479 reduction in matric suction that highlights the material's sensitivity to failure induced by rainfall.
480 The material is also found to hold enough moisture during wetting and drying processes i.e.,
481 rainfall and evaporation.

482 **5.2 Entry into the list of largest debris flows in India**

483 Debris flows are common in mountainous India, especially in the Himalayas and the Western
484 Ghats during heavy monsoon rains or cloudbursts. While channelized debris flows are more
485 frequent in the Western Ghats, the Himalayas experience more rock fall-evolved debris flows
486 (Abraham et al., 2024). The July 2024 Wayanad debris flow, with an estimated volume of 5.1 to
487 5.7 million cubic meters (MCM), ranks among the largest debris flow events in recent Indian
488 history. This event caused extensive damage and loss of life in the Chaliyar River Valley, triggered
489 by intense rainfall and the region's geologically unstable terrain. It is notable not only for its size
490 but also for its devastating impact on both human settlements and the environment.

491
492 By comparison, other major debris flows in India include the Malpa landslide, which occurred on
493 August 18, 1998. This complex landslide, initiating as a rockslide and evolving into a debris flow,
494 was triggered by prolonged heavy precipitation. The runout distance was about 900 m with a
495 maximum width of approximately 800 m. Although Malpa was one of India's deadliest landslides,
496 its debris volume was significantly lower, around 1 MCM (Paul et al., 2000). Similarly, the

497 Pettimudi landslide (2020) and Kuricherrmala landslide (2018), despite their severe runout
498 distances (1.2 km and 3.1 km respectively), had smaller volumes of 280,000 m³ (Achu et al.,
499 2021).

500
501 While the Wayanad debris flow is one of the largest known debris flows in terms of volume in
502 India, it pales in comparison to the Chamoli disaster of February 2021 which is a rock-ice
503 avalanche debris flow and the Kotrupi landslide (2017), a debris flow. Kotrupi landslide in
504 Himachal Pradesh, during 2017, claimed more than 50 lives (Singh et al. 2020) and involved an
505 estimated 5.9×10^6 m³ of debris (Prajapati and Jaboyedoff, 2022), a slightly higher volume than
506 the Wayanad event. These landslides, like Wayanad, were all triggered by extreme weather and
507 local geology in mountainous regions with deeply weathered and fractured bedrock. However,
508 Wayanad's debris flow, with a runout distance of about 8 km, demonstrates the immense
509 erosional power and sediment transport capacity associated with large-scale flows in regions
510 where geological, geomorphological and climatic factors converge to create ideal conditions for
511 catastrophic events. Our geotechnical analysis supports this argument with the identified
512 presence of finer sized grains in the debris flow deposits of Wayanad. Studies have shown
513 presence of finer grains in channel/bed deposits will result in more erosion (Domènech et al.,
514 2019, Yang et al., 2023). The median grain size (D_{50}) of Wayanad debris flow obtained from
515 laboratory sieving is four times smaller than events in the Himalayas i.e., the 2013 Kedarnath and
516 the 2021 Chamoli debris flows (Dewrari and Sivasubramanian, 2023). This factor could be a
517 reason for the huge volume of the debris flow that occurred in Wayanad. In addition, the presence
518 of debris from previously occurred landslides could have aided to the volume through entrainment
519 during the flow (Jakob et al., 2005; Iverson, 2011).

520
521 The Chamoli event in the Uttarakhand Himalayas, involved a staggering 27 MCM of material.
522 Though this event had a different trigger mechanism—believed to be a combination of rockfall,
523 and glacial collapse, it shares similarities with debris flows in terms of the downstream damage
524 caused by the mass movement of material. The massive runout caused by the Chamoli avalanche
525 destroyed two hydroelectric plants and caused major flooding, which is a comparable downstream
526 impact to the deposition and flooding risks following the Wayanad debris flow. Despite the scale
527 differences, a comparative analysis highlights the range of factors contributing to these
528 catastrophic events across India's varied landscapes. The Wayanad event exemplifies how
529 changes in rainfall patterns, combined with geological instability, can produce disasters of
530 unprecedented magnitude in tropical and subtropical settings. It emphasizes the need for more
531 robust monitoring and preparedness strategies in high-risk zones across India, as both types of
532 events pose significant hazards to lives, infrastructure, and ecosystems.

533 534 **5.3 Precursors, key to early hazard detection and mitigation**

535 Precursor events leading up to major landslides have been observed in all the cases mentioned,
536 including the Wayanad, Chamoli, Kotrupi, and Malpa events. This underscores the critical
537 importance of continuously monitoring small-scale events in populated areas using Internet of
538 Things (IoT)-based, low-cost EWS to help prevent disasters. For example, in Wayanad, a
539 significant landslide occurred in 2020 following heavy monsoon rains, destabilizing slopes and
540 depositing debris and large boulders in the river valley. In 1984, a debris flow was triggered at an
541 altitude of 860 m in the same stream with a runout of 1.5 km which generated 9,50,000 cubic
542 meters of debris and killed 14 people (Basak and Prasad, 1985, 1989). These smaller
543 occurrences should have served as early warning signs for the larger debris flow that took place
544 in 2024. Indeed, the vulnerability of Mundakkai as a landslide-prone area was recognized early
545 on (Muraleedharan, 1995; Kuriakose et al., 2009). In 2007, Kuriakose et al. (2008) conducted soil
546 strength parameterization of the crown area and modeled the runout of the 1984 event. After the

547 2020 landslide, the local government developed a Disaster Management Plan, identifying
548 Mundakkai, Punchirimattom, and parts of Vellarimala as high-risk zones (MGP, 2019).

549
550 An evacuation drive was initiated at 5 a.m. on August 29, following a minor landslide earlier that
551 morning, with the District Panchayat President, co-chair of the district disaster management
552 authority, Aapda Mitra Volunteers (the official disaster management volunteers trained by
553 Disaster Management Authorities), Police, Revenue Officials and Local Government aiding in the
554 evacuation and alerting residents living in Punchirimattam, Mundakkai and Chooralmala
555 settlements mainly along the river banks, and restricting tourist access to Chooralmala area,
556 which is evident from various new reports in Malayalam, the local vernacular (Mathrubhumi News,
557 2024; Manorama News, 2024). Many individuals, noticing the rainfall and the presence of officials
558 intuitively moved to safer areas. The anticipatory actions and the intuitions of locals saved many
559 precious lives. However, the magnitude of the July 30, 2024, event was unprecedented,
560 particularly so in the devastation that the event caused in Chooralmala settlement over 6 kms
561 from the triggering zone, situated in the valley area. The most impacted part of Chooralmala
562 settlement is about 80 meters away from the river bank and had not experienced the direct impact
563 of a landslide in over one century of its existence as a human habitation.

564
565 At the confluence of Punapuzha with Vellarimala stream near Chooralmala settlement, the back
566 wash can be seen up to 100 m from the confluence point into the Vellarimala stream destroying
567 buildings located 60 m above the river bed of this stream. This confluence of Vellarimala stream
568 with the debris carrying Punapuzha may have further reduced the viscosity of the debris resulting
569 in the breach of bank along the Chooralmala School Road, causing destruction in the area with
570 no near history of landslide impact. This area of about 1 km² with over 100 houses is now buried
571 in a pile of large boulders and debris. This complexity also implies that the scope of runout
572 modelling carried out needs to be further increased and other rheological models tested to
573 optimize the most appropriate model for utilizing in probabilistic hazard mapping.

574
575 Similar to the Wayanad event, the Chamoli region also experienced a significant landslide in 2016,
576 which destabilized the slope and created surface cracks (Fan et al., 2021). These conditions
577 contributed to the devastating ice-rock avalanche in 2021. The Kotrupi landslide in Himachal
578 Pradesh was also preceded by multiple events in 1977 and 1997, which caused slope failures
579 and gradual slope destabilization. This slow weakening of the landscape eventually culminated in
580 the 2017 landslide, when heavy rains triggered a major collapse, leading to several fatalities. In
581 Malpa, small landslides just two days before the catastrophic event that claimed over 200 lives
582 served as clear warnings of an impending disaster. These examples highlight that smaller,
583 precursor landslides are critical indicators of a region's increasing vulnerability to larger, more
584 destructive events. Recognizing these early signs, implementing proactive monitoring systems,
585 and adopting appropriate landuse in runout zones is essential to mitigate future disasters and
586 protect communities in landslide-prone areas.

587 588 **5.4 Challenges for developing LEWS**

589 Extreme rainfall events (ERE) are the primary trigger for landslides in the Western Ghats, making
590 the region a hotspot for climate change-related impacts (Kuriakose et al., 2009). Forecasting
591 EREs remains a significant challenge, with the main source of uncertainty being the accurate
592 representation of associated physical processes (Merino et al., 2022). At present, no operational
593 landslide early warning system except an experimental system of Geological Survey of India (GSI)
594 was available for the study area. The system implemented by GSI uses a regional rainfall
595 threshold-based approach for issuing experimental forecasts which is in a testing stage and is not
596 operationally available. This forecast from GSI heavily depends on the rainfall forecast.

597 A recent study by Singh et al. (2024) assessed the performance of Weather Research and
598 Forecasting (WRF) models in simulating the extreme rainfall that led to the 2024 Wayanad
599 landslide. Their analysis of two WRF simulations revealed that stations with higher rainfall
600 consistently showed increased RMSE values, indicating reduced model reliability in capturing
601 extreme rainfall events.

602 While the model's overall performance varied with rainfall intensity, a consistent underestimation
603 of extreme rainfall highlights the need for improvements, especially in predicting events like
604 Wayanad. The study concluded that enhancing the parameterization of cloud microphysics,
605 planetary boundary layer, and surface layer schemes could improve the model's sensitivity to
606 extreme rainfall. This also underscores why no red alert was issued for the region prior to the
607 event, suggesting that global factors influencing the monsoon were neutral during the event and
608 that the local conditions drove the extreme rainfall on July 29 and 30.

609 In the absence of accurate forecasts, localizing the space and time of landslides, especially debris
610 flows by Territorial Landslide Early Warning Systems (Te-LEWS) is difficult due to non-availability
611 of slope-scale weather information and demonstrated hydro-meteorological thresholds (Dixit et.,
612 al. 2024). Therefore, it is essential to test different hydro-meteorological thresholds like the Soil-
613 Water Index (SWI) which holds information of real-time hydrology of the terrain (Sivasubramanian
614 et al., 2023) and proven successful in mitigating sediment disaster in nations like Japan, Taiwan
615 and Sri Lanka (Osanai et al., 2010; Chen et. al., 2017; Gamage et. al., 2021).

616 **Conclusion**

617 Landslides in the Western Ghats Mountain ecosystem have been increasing in frequency and
618 severity, driven by extreme rainfall events and the region's inherent geological fragility. These
619 events result in significant economic losses and pose ongoing threats to life and infrastructure.
620 Documenting the causes and consequences of large, fatal landslides is critical for developing
621 effective risk mitigation and adaptation strategies; and one of the most pressing research needs
622 is for developing complete landslide inventories and documentation for events in a wider
623 geographical environment.

624 In this study, we conducted a detailed investigation into the causes of the catastrophic Wayanad
625 landslide that occurred on July 30, 2024, claiming 239 lives and causing extensive damage to
626 infrastructure. Our analysis employed a combination of field surveys, satellite image analysis,
627 laboratory testing, and aerial surveys. The aerial surveys, conducted using UAVs, captured
628 detailed geometry and textural information of the landslide, providing a solid foundation for
629 documentation. When combined with LiDAR data, the resulting orthomosaics and digital elevation
630 models (DEMs) enabled us to map fine-scale geological features and identify structural
631 weaknesses with high precision.

632 Our analysis reveals that the Wayanad landslide is one of the largest in India in terms of volume,
633 runout distance, and fatalities, and it originated from a preexisting fracture formed during the 2020
634 event. The 2024 landslide was the culmination of a cascading sequence of geological processes.
635 It began with the progressive widening of cracks in the slope, which led to a planar rock failure,
636 exacerbated by water pressure from intense rainfall. This failure transitioned into a highly mobile
637 debris flow, further intensified by the damming effect of accumulated material and the area's steep
638 topography. The combination of these factors created ideal conditions for the catastrophic
639 landslide. Field observations and aerial imagery support our conclusion that the landslide was not
640 of anthropogenic origin, as some media reports have suggested. Instead, the event was primarily
641 caused by a combination of geological and structural factors, triggered by an intense monsoon
642 spell. The data and insights presented in this study provide a crucial baseline for future research,

643 enabling more effective disaster preparedness and risk mitigation strategies in similar
644 environments.

645 **Acknowledgements**

646 We acknowledge Shagin Sunny and Vishnu KM and others who have shared videos and images
647 of pre and post event in the social media platforms (Facebook, Instagram, YouTube, and X). We
648 are grateful to PlanetLabs for rapid data access, and Marc Christen for providing the RAMMS
649 License. This work was supported by ISRO-DMSP by a research grant IIRS/DO/DMSP-
650 ASCB/AS/2023/06 (APY and KSS). APY thanks IISER Mohali for the UAV & LIDAR facilities. APY
651 also thank Prof. Sanjay Mondal and his students, IISER Mohali for generating the XRD spectrum.

652 **Funding**

653 This research received travel support from ISRO-DMSP (Grant No: IIRS/DO/DMSP-
654 ASCB/AS/2023/06) for Ali P. Yunus¹ and K.S. Sajinkumar².

655 **Competing interests:**

656 The authors declare that they have no competing interests.

657 **Author contributions**

658 APY designed the study, performed the field visit, drone surveys and image processing and
659 drafted the manuscript content along with KSS, SLK, TO, and SSS. KSS obtained the necessary
660 permission for the fieldwork and performed the field visits and in-situ geological observations. GG
661 took part in the initial fieldwork and drone surveys, and contributed the geomorphological
662 investigations. SSS performed the numerical analysis for stability and debris flow initiation with
663 inputs from MD, SD, and JT. SK, JT, ALA, AI, VKP, and AR all assisted in the fieldwork, drone
664 surveys, and in-situ sample collection, and experiments for geotechnical experiments. SMUI run
665 the RAMMS modeling, and MD performed the geotechnical experiments. SD collected the
666 meteorological data for modelling together with SuS. ShS and PS analyzed the meteorological
667 forecasts. NNV assisted in geotechnical characterization and numerical analysis. ACN, VA, GSP
668 and SLK assisted in conceptualizing the study. SLK administered necessary official procedures
669 for field work and contributed to the conceptualization. All authors have contributed to the writing
670 of this work.

671 **Data and materials availability:** All data are available upon request.

672 **References**

673 ABPLive. (2024, August 3). "Communist-Congress made disaster": BJP MP Tejasvi Surya calls
674 Wayanad landslides "Man-Made" tragedy. <https://news.abplive.com>.
675 [https://news.abplive.com/states/kerala/wayanad-landslides-tejasvi-surya-communist-congress-](https://news.abplive.com/states/kerala/wayanad-landslides-tejasvi-surya-communist-congress-made-disaster-bjp-mp-calls-man-made-tragedy-1707808)
676 [made-disaster-bjp-mp-calls-man-made-tragedy-1707808](https://news.abplive.com/states/kerala/wayanad-landslides-tejasvi-surya-communist-congress-made-disaster-bjp-mp-calls-man-made-tragedy-1707808)

677 Abolmasov, B., Milenković, S., Marjanović, M., Đurić, U., & Jelisavac, B. (2015). A geotechnical
678 model of the Umka landslide with reference to landslides in weathered Neogene marls in Serbia.
679 *Landslides*, 12, 689-702.

680 Abraham, M. T., & Satyam, N. (2024). Need for Detailed Landslide Inventory Maps and Landslide
681 Databases in Indian Context. In *Civil Engineering Innovations for Sustainable Communities with*
682 *Net Zero Targets* (pp. 277-296). CRC Press.

- 683 Achu, A. L., Joseph, S., Aju, C. D., & Mathai, J. (2021). Preliminary analysis of a catastrophic
684 landslide event on 6 August 2020 at Pettimudi, Kerala State, India. *Landslides*, 18, 1459-1463.
- 685 Achu, A. L., Thomas, J., Aju, C. D., Vijith, H., & Gopinath, G. (2024). Redefining landslide
686 susceptibility under extreme rainfall events using deep learning. *Geomorphology*, 448, 109033.
- 687 Ambili, V., & Narayana, A. C. (2022). River drainage response to tectonism: Evidence from the
688 Chaliyar river basin, southwestern India. *Journal of Earth System Science*, 131(2), 96.
- 689 Basak P, Prasad NBN (1985) Landslides in the Western Ghats. In: Proceedings of the workshop
690 on landslides in Western Ghats, 30–31 July 1985, Kozhikode, India. Kerala State Committee on
691 Science, Technology and Environment.
- 692 Basak P, Prasad NBN (1989) Recurring landslides in the Western Ghats—an environmental
693 hazard. *Environ Conserv* 16(2):169–172
- 694 Chen, C. W., Saito, H., & Oguchi, T. (2017). Analyzing rainfall-induced mass movements in
695 Taiwan using the soil water index. *Landslides*, 14, 1031-1041.
- 696 Cheng, Z., Gong, W., Tang, H., Juang, C. H., Deng, Q., Chen, J., & Ye, X. (2021). UAV
697 photogrammetry-based remote sensing and preliminary assessment of the behavior of a landslide
698 in Guizhou, China. *Engineering Geology*, 289, 106172.
- 699 Cruden, D. (1991). A suggested method for a landslide summary. *Bulletin of Engineering Geology
700 & the Environment*, 43(1).
- 701 Dai, C., Higman, B., Lynett, P. J., Jacquemart, M., Howat, I. M., Liljedahl, A. K., ... & Haeussler,
702 P. J. (2020). Detection and assessment of a large and potentially tsunamigenic periglacial
703 landslide in Barry Arm, Alaska. *Geophysical Research Letters*, 47(22), e2020GL089800.
- 704 Dai, C., Howat, I. M., van der Sluijs, J., Liljedahl, A. K., Higman, B., Freymueller, J. T., ... & Marsh,
705 P. (2024). Applications of ArcticDEM for measuring volcanic dynamics, landslides, retrogressive
706 thaw slumps, snowdrifts, and vegetation heights. *Science of Remote Sensing*, 9, 100130.
- 707 Dai, F. C., Lee, C. F., & Ngai, Y. Y. (2002). Landslide risk assessment and management: an
708 overview. *Engineering geology*, 64(1), 65-87.
- 709 Das, P. (2024, August 6). Kerala government to blame for Wayanad disaster: Union minister.
710 *Mint*. [https://www.livemint.com/politics/kerala-landslides-deaths-rainfall-development-projects-
711 wayanad-disaster-bhupender-yadav-11722866682817.html](https://www.livemint.com/politics/kerala-landslides-deaths-rainfall-development-projects-wayanad-disaster-bhupender-yadav-11722866682817.html)
- 712 Detert, M., & Weitbrecht, V. (2013). User guide to gravelometric image analysis by BASEGRAIN.
713 *Advances in science and research*, 1789-1795.
- 714 Dewrari, M., & Siva Subramanian, S. (2023, May). Correlating grain-size distributions, transport
715 mechanism, and runout distance of debris flow deposits in the Himalayas. In EGU General
716 Assembly Conference Abstracts (pp. EGU-13031).
- 717 Dixit, S., Siva Subramanian, S., Srivastava, P., Yunus, A. P., Martha, T. R., & Sen, S. (2024).
718 Numerical-model-derived intensity–duration thresholds for early warning of rainfall-induced debris
719 flows in a Himalayan catchment. *Natural Hazards and Earth System Sciences*, 24(2), 465-480.

- 720 Domènech, G., Fan, X., Scaringi, G., van Asch, T. W., Xu, Q., Huang, R., & Hales, T. C. (2019).
721 Modelling the role of material depletion, grain coarsening and revegetation in debris flow
722 occurrences after the 2008 Wenchuan earthquake. *Engineering Geology*, 250, 34-44.
- 723 Fan, X., Yunus, A. P., Yang, Y. H., Subramanian, S. S., Zou, C., Dai, L., ... & Huang, R. (2022).
724 Imminent threat of rock-ice avalanches in High Mountain Asia. *Science of the Total Environment*,
725 836, 155380.
- 726 Fehr, R. (1987). Einfache Bestimmung der Korngrößenverteilung von Geschiebematerial mit
727 Hilfe der Linienzahlanalyse (Simple detection of grain size distribution of sediment material using
728 line-count analysis). *Schweizer Ingenieur und Architekt*, 105(38), 1104–1109 (in German).
- 729 Froude, M. J., & Petley, D. N. (2018). Global fatal landslide occurrence from 2004 to 2016. *Natural
730 Hazards and Earth System Sciences*, 18(8), 2161-2181.
- 731 Gadgil, M. (2014). Western Ghats ecology expert panel: a play in five acts. *Economic and Political
732 Weekly*, 38-50.
- 733 Gamage, H. G. C. P., Wada, T., Senadeera, K. P. G. W., Aroos, M. S. M., & Bandara, D. M. L.
734 (2021). Rainfall Triggered Landslide Early Warning System Based on Soil Water Index. In *Multi-
735 Hazard Early Warning and Disaster Risks* (pp. 529-542). Springer International Publishing.
- 736 Gutiérrez, F., Soldati, M., Audemard, F., & Bălteanu, D. (2010). Recent advances in landslide
737 investigation: Issues and perspectives. *Geomorphology*, 124(3-4), 95-101.
- 738 Guzzetti, F. (2019). Iverson, R. M., Reid, M. E., Logan, M., LaHusen, R. G., Godt, J. W., & Griswold,
739 J. P. (2011). Positive feedback and momentum growth during debris-flow entrainment of wet bed
740 sediment. *Nature Geoscience*, 4(2), 11600). Landslide fatalities and the evaluation of landslide
741 risk in Italy. *Engineering geology*, 58(2), 89-107.
- 742 Guzzetti, F., Mondini, A. C., Cardinali, M., Fiorucci, F., Santangelo, M., & Chang, K. T. (2012).
743 Landslide inventory maps: New tools for an old problem. *Earth-Science Reviews*, 112(1-2), 42-
744 66.
- 745 Jakob, M., Hungr, O., Hungr, O., McDougall, S., & Bovis, M. (2005). Entrainment of material by
746 debris flows. *Debris-flow hazards and related phenomena*, 135-158.
- 747 Klose, M., Highland, L., Damm, B., & Terhorst, B. (2014). Estimation of direct landslide costs in
748 industrialized countries: Challenges, concepts, and case study. In *Landslide Science for a Safer
749 Geoenvironment: Volume 2: Methods of Landslide Studies* (pp. 661-667). Springer International
750 Publishing.
- 751 Kerala State Disaster Management Authority (KSDMA). (2014). Handbook on Emergency
752 Operations – Volume 1 – Hazard Susceptible Areas of Kerala; Government Publication
753 (https://sdma.kerala.gov.in/wp-content/uploads/2018/11/ILDM_2014.pdf)
- 754 Kuriakose, S.L., Sankar, G., Muraleedharan C, (2009). History of landslide susceptibility and a
755 chorology of landslide-prone areas in the Western Ghats of Kerala, India, *Environ Geol* 57, 1553–
756 1568. <https://doi.org/10.1007/s00254-008-1431-9>

757 Kuriakose, S. L., Van Beek, L. P. H., & Van Westen, C. J. (2009). Parameterizing a physically
758 based shallow landslide model in a data poor region. *Earth surface processes and landforms*,
759 34(6), 867-881.

760 Xiao Li, Huayong Chen, Xiaoqing Chen, Tao Wang, Yao Jiang, Hechun Ruan, (2024).
761 Experimental study on the stability of noncohesive landslide dams based on seepage effect,
762 *Engineering Geology*, 341, <https://doi.org/10.1016/j.enggeo.2024.107708>.

763 Lin, M. L., Chen, Y. C., Tseng, Y. H., Chang, K. J., & Wang, K. L. (2021). Investigation of
764 geological structures using UAV LiDAR and its effects on the failure mechanism of deep-seated
765 landslide in Lantai Area, Taiwan. *Applied Sciences*, 11(21), 10052.

766 Lindner, G., Schraml, K., Mansberger, R., & Hübl, J. (2016). UAV monitoring and documentation
767 of a large landslide. *Applied Geomatics*, 8, 1-11.

768 Lissak, C., Bartsch, A., De Michele, M., Gomez, C., Maquaire, O., Raucoules, D., & Roulland, T.
769 (2020). Remote sensing for assessing landslides and associated hazards. *Surveys in*
770 *Geophysics*, 41(6), 1391-1435.

771 Mathrubhumi News, 29-7-2024, Report on heavy rainfall and local flooding in Mundakkai,
772 Chooralmala area and anticipatory actions. <https://youtu.be/BzWDpUQENts>

773 Manorama News, 29-7-2024, Report on heavy rainfall and possible small debris flow in
774 Punapuzha and anticipatory actions. <https://youtu.be/BzWDpUQENts>

775 Meppadi Grama Panchayath (MGP). (2019). Disaster Management Plan of Meppadi Grama
776 Panchayath 2019; Government Publication ([https://dmp.kila.ac.in/maps/Wayanad/1096-](https://dmp.kila.ac.in/maps/Wayanad/1096-Meppadi_GP/Disaster_Management_Plan_Document_2019.pdf)
777 [Meppadi_GP/Disaster_Management_Plan_Document_2019.pdf](https://dmp.kila.ac.in/maps/Wayanad/1096-Meppadi_GP/Disaster_Management_Plan_Document_2019.pdf))

778 Muraleedharan MP (1995) Landslides in Kerala—a drenched state phenomena in regolith. In:
779 Abstracts of the national seminar on landslides in Western Ghats, 29–30 Aug 1995.

780 Niethammer, Uwe, M. R. James, Sabrin Rothmund, Julien Travelletti, and Manfred Joswig. "UAV-
781 based remote sensing of the Super-Sauze landslide: Evaluation and results." *Engineering*
782 *Geology* 128 (2012): 2-11.

783 Osanai, N., Shimizu, T., Kuramoto, K., Kojima, S., & Noro, T. (2010). Japanese early-warning for
784 debris flows and slope failures using rainfall indices with Radial Basis Function Network.
785 *Landslides*, 7, 325-338.

786 Paul, S. K., Bartarya, S. K., Rautela, P., & Mahajan, A. K. (2000). Catastrophic mass movement
787 of 1998 monsoons at Malpa in Kali Valley, kumaun Himalaya (India). *Geomorphology*, 35(3-4),
788 169-180.

789 Petley, D. (2012). Global patterns of loss of life from landslides. *Geology*, 40(10), 927-930.

790 Prajapati, G., & Jaboyedoff, M. (2022). Method to estimate the initial landslide failure surface and
791 volumes using grid points and spline curves in MATLAB. *Landslides*, 19(12), 2997-3008.

792 RAMMS (2017). *RAMMS::DEBRISFLOW User Manual*. Davos, Switzerland: ETH Available at:
793 https://ramms.slf.ch/ramms/downloads/RAMMS_DBF_Manual.pdf.

794 Reuters. (2024) <https://www.reuters.com/graphics/ASIA-WEATHER/INDIA->
795 [LANDSLIDE/gdvzmgkenpw/](https://www.reuters.com/graphics/ASIA-WEATHER/INDIA-LANDSLIDE/gdvzmgkenpw/)

796 Rothmund, S., Vouillamoz, N., & Joswig, M. (2017). Mapping slow-moving alpine landslides by
797 UAV—Opportunities and limitations. *The Leading Edge*, 36(7), 571-579.

798 Sajinkumar, K. S., & Oommen, T. (2021). Landslide atlas of Kerala. *GSI Publications*, 7(1).

799 Sajit. C.P. (2024.). *Kerala's Wayanad Landslide: Wayanad disaster man-made, says Madhav*
800 *Gadgil, blames Kerala government for ignoring ecological recommendations*. The Hindu.
801 [https://www.thehindu.com/news/national/kerala/wayanad-disaster-man-made-says-madhav-](https://www.thehindu.com/news/national/kerala/wayanad-disaster-man-made-says-madhav-gadgil-blames-kerala-government-for-ignoring-ecological-recommendations/article68463667.ece)
802 [gadgil-blames-kerala-government-for-ignoring-ecological-](https://www.thehindu.com/news/national/kerala/wayanad-disaster-man-made-says-madhav-gadgil-blames-kerala-government-for-ignoring-ecological-recommendations/article68463667.ece)
803 [recommendations/article68463667.ece](https://www.thehindu.com/news/national/kerala/wayanad-disaster-man-made-says-madhav-gadgil-blames-kerala-government-for-ignoring-ecological-recommendations/article68463667.ece)

804 Shugar, D. H., Jacquemart, M., Shean, D., Bhushan, S., Upadhyay, K., Sattar, A., ... & Westoby,
805 M. J. (2021). A massive rock and ice avalanche caused the 2021 disaster at Chamoli, Indian
806 Himalaya. *Science*, 373(6552), 300-306.

807 Singh S., Piyush S., Anandu P., Srikrishnan S.S., A.P. Yunus (2024). Numerical Weather
808 Prediction Model Underestimated the Extent of Extreme Rainfall Event during the 2024 Wayanad
809 (Kerala, India) Landslide. *Natural Hazards and Earth System Sciences (NHES)* (Pre-print).

810 Singh, N., Gupta, S. K., & Shukla, D. P. (2020). Analysis of landslide reactivation using satellite
811 data: a case study of Kotrupi landslide, Mandi, Himachal Pradesh, India. *The International*
812 *Archives of the Photogrammetry, Remote Sensing and Spatial Information Sciences*, 42, 137-
813 142.

814 Siva Subramanian, S., Sen, S., & Yunus, A. P. (2023, May). Applicability of complex rainfall
815 thresholds for Territorial Landslide Early Warning Systems (Te-LEWS) in the Himalayas. In EGU
816 General Assembly Conference Abstracts (pp. EGU-16763).

817 Valkaniotis, S., Papathanassiou, G., & Ganas, A. (2018). Mapping an earthquake-induced
818 landslide based on UAV imagery; case study of the 2015 Okeanos landslide, Lefkada, Greece.
819 *Engineering geology*, 245, 141-152.

820 Van Westen, C. J., & Getahun, F. L. (2003). Analyzing the evolution of the Tessina landslide using
821 aerial photographs and digital elevation models. *Geomorphology*, 54(1-2), 77-89.

822 Yang, F., Fan, X., Wei, Z., Subramanian, S. S., Van Asch, T. W., & Xu, Q. (2023). Modelling the
823 evolution of debris flows after the 2008 Wenchuan earthquake. *Engineering Geology*, 321,
824 107152.

825 Yunus, A. P., Fan, X., Subramanian, S. S., Jie, D., & Xu, Q. (2021). Unraveling the drivers of
826 intensified landslide regimes in Western Ghats, India. *Science of the total environment*, 770,
827 145357.

828

829